Nano Energy 131 (2024) 110293

Contents lists available at ScienceDirect

Nano Energy

journal homepage: www.elsevier.com/locate/nanoen

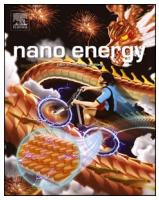

Vertical heterostructures for symmetrical and reversible solid oxide fuel cells

Javier Zamudio-García [a,b,*], Francesco Chiabrera [a], Enrique R. Losilla [b], David Marrero-López [c], Vincenzo Esposito [a,**]

[a] Department of Energy Conversion and Storage, Technical University of Denmark, Fysikvej, Building 310, Kgs. Lyngby 2800, Denmark
[b] Universidad de Málaga, Dpto. de Química Inorgánica, Cristalografía y Mineralogía, Málaga 29071, Spain
[c] Universidad de Málaga, Dpto. de Física Aplicada I, Málaga 29071, Spain

ARTICLE INFO

Keywords:
VAN
Solid oxide fuels cells
Ceria
Ferrite
Thin films
Functional metal oxides

ABSTRACT

Interfacial modification using functional metal oxides holds great potential for enhancing the electrochemical performance of solid oxide fuel cells (SOFCs). This study presents a redox-stable vertically aligned nanostructure (VAN) thin film based on a heteroepitaxial perovskite-fluorite nanocomposite prepared by pulsed laser deposition on different substrates. The self-assembled functional layers consist of alternating columns of two well-differentiated phases, $(La_{0.8}Sr_{0.2})_{0.95}Fe_{0.8}Ti_{0.2}O_{3-\delta}$-$Ce_{0.9}Gd_{0.1}O_{1.95}$ (LSFT-CGO) VAN, with multiple strained vertical interfaces. The coexistence of two immiscible phases at the nanoscale significantly extends the triple phase boundary (TPB) and reaction sites, resulting in fast electrochemical redox reactions. The LSFT-CGO VAN active layer demonstrates improved performance under both air and H_2 conditions, with polarization resistances of 2.9 and 75.9 Ω cm^2 at 650 °C, respectively. The nanoengineering design of functional metal oxides featuring hierarchical columnar architecture represents a significant step towards developing efficient energy conversion devices, particularly symmetrical and reversible SOFCs.

1. Introduction

Solid oxide fuel cells (SOFC) have garnered significant attention as a promising option for the reversible conversion of chemical energy into electrical energy [1,2]. However, their operating temperatures are still high (≥ 800 °C), leading to substantial degradation over time and comprising the structural integrity of the cells [3,4]. In recent years, extensive research has been done to lower the operating temperature through nanoengineering approaches at the electrode/electrolyte interface [5,6]. Incorporating a thin functional layer has enhanced ion transport, oxygen reduction kinetics, and improved contact between the cell components [6–8]. Pulsed laser deposition (PLD) has proven to be an effective technique for the preparation of dense epitaxial functional layers for fabricating energy-conversion devices [9–11]. In Solid Oxide Cells, PLD is extensively used in intermediate-temperature SOFCs operating at 500–700 °C, offering precise control over the film quality, physical properties, and morphology [12,13]. Particularly, it is attracting great attention in μ-SOFCs [14,15]. Moreover, PLD enables the fabrication of cell components in a short time at low temperatures without the need for post-thermal treatment of the as-deposited films.

Traditionally, composite materials have improved the electrochemical properties of the oxygen reduction and fuel oxidation reaction in SOFCs. Typically, these composites are formed by an electrode with high electronic conductivity mixed with oxide-ion conductors to extend the triple-phase boundary (TPB) [16,17]. Several reports have demonstrated that incorporating dense active layers deposited via PLD significantly enhances the contact between the air electrode and electrolyte. Therefore, the main function of an active layer is to improve the electrical connection between the electrolyte and electrodes, resulting in a notable enhancement of the electrochemical processes at the interphase and, consequently, improving electrode performance [12,13].

In this context, heteroepitaxial films, particularly vertically aligned nanostructures (VAN), have emerged as one of the most promising approaches for obtaining nanocomposite heterostructures for energy applications [18,19]. Additionally, by employing strain engineering, the design of VAN oxide-based heterostructures has shown superior

* Corresponding author at: Department of Energy Conversion and Storage, Technical University of Denmark, Fysikvej, Building 310, Kgs. Lyngby 2800, Denmark.
** Corresponding author.
E-mail addresses: javzam@dtu.dk (J. Zamudio-García), vies@dtu.dk (V. Esposito).

https://doi.org/10.1016/j.nanoen.2024.110293
Received 20 March 2024; Received in revised form 26 August 2024; Accepted 22 September 2024
Available online 24 September 2024

performance in diverse fields, including ferroelectrics, magnetic materials, ionic conductors and fuel cells [11,14,20–23]. The nanoengineering of self-assembly VANs enables vertical lattice strain due to the coexistence of two phases with out-of-plane coherence. The unique hierarchical columnar architecture of the VAN, with its high density of interphases on the surface, significantly enlarges the TPB for electrochemical reactions compared to conventional single-phase films. [5,24,25]. Most importantly, the VAN layer promotes faster electrochemical reactions at the interface and provides coherent out-of-plane transport pathways for both oxide ions and electrons.

The architecture and microstructure of the film are known to significantly influence the electrochemical properties of thin-film-based SOFCs [25,26]. In this context, the primary function of VANs films is to serve as active layers rather than solely as electrodes. In recent years, outstanding improvement in cell performance has been reported by implementing VANs as active layers for air electrode materials, such as $La_{0.8}Sr_{0.2}MnO_{3-\delta}$-$Ce_{0.8}Sm_{0.2}O_{1.9}$ (LSM-SDC) [27], $La_{0.8}Sr_{0.2}CoO_{3-\delta}$-$Ce_{0.9}Gd_{0.1}O_{1.95}$ (LSC-CGO) [28], $La_{0.6}Sr_{0.4}Co_{0.2}Fe_{0.8}O_{3-\delta}$-$Ce_{0.9}Gd_{0.1}O_{1.95}$ (LSCF-CGO) [29], LSC/ $(La_{0.5}Sr_{0.5})_2CoO_4$ [30] or $PrBaCo_2O_{5+\delta}$-CGO [31]. Additionally, VANs have been implemented in different SOFC configurations, in anode-supported [29], electrolyte-supported [32] or metal-supported cells [11]. Metal-supported configurations are particularly promising due to the use of a thin electrolyte with symmetrical electrodes supported by metal, which helps to reduce ohmic losses and enables operation at lower temperatures [11]. For instance, Baiutti et al. observed a stable polarization resistance (R_p) of ~ 6 Ω cm^2 at 700 °C for an LSM-SDC VAN, which avoided the dopant segregation on the surface observed in the LSM layer (~400 Ω cm^2) [27]. Recently, Develos-Bagarinao et al. confirmed the successful implementation of a self-assembled LSCF-CGO active layer with a columnar microstructure deposited by PLD on polycrystalline electrolytes [29]. Incorporating this functional layer in a Ni-YSZ/YSZ/CGO half-cell with LSC electrodes significantly outperformed the reference cell, achieving an outstanding peak power density of 3.3 W cm^{-2} at 700 °C and demonstrating excellent durability. Additionally, the LSCF-SDC vertically aligned nanocomposite deposited by PLD was recently implemented on aluminum oxide substrates for SOFCs [11]. Kang et al. also prepared a columnar SSC-CGO thin film by PLD on polycrystalline $La_{0.9}Sr_{0.1}Ga_{0.8}Mg_{0.2}O_{3-\delta}$/SDC electrolytes achieving a high peak of power density of 1075 mW cm^{-2} at 600 °C in wet H_2 [32].

However, most studies have primarily focused on VAN functional layers for air electrodes, where the electronic conductor phase with perovskite-type structure exhibits low redox stability, limiting their application in reducing conditions [33]. The preparation of redox-stable VANs holds a great potential not only to improve the electrochemical activity in both oxidizing and reducing conditions but also to facilitate reversible operation, minimizing poisoning of the electrodes and degradation [34,35]. Robust redox stability is of utmost importance in counteracting cell degradation processes associated with sulphur poisoning or carbon deposition, which can be mitigated by reversing the feeding gases into the cell [34,35]. These layers are highly promising for implementation in symmetrical SOFCs, where the electrode on the air and fuel sides has the same composition [36].

$La_{1-x}Sr_xFeO_{3-\delta}$-based perovskites doped with cations exhibiting superior redox stability are considered one of the most promising mixed conductors for efficient operation as symmetrical electrodes [37]. Among these candidates, Ti-doped ferrites have shown remarkable potential as air and fuel electrodes, demonstrating good performance and stability under long operation times [38–42]. Recent works by Hou et al. have reported excellent electrochemical performance for $La_{0.3}Sr_{0.7}Fe_{0.9}Ti_{0.1}O_{3-\delta}$ working in air and H_2 atmospheres in fuel cell and electrolysis modes [38,43]. These findings indicate that implementing advanced heteroepitaxial functional layers based on Ti-doped ferrites has great potential for enhancing electrochemical performance in both oxidizing and reducing conditions.

In this study, we propose an innovative vertically aligned nanostructure (VAN) consisting of alternating columns of perovskite and fluorite phases, $(La_{0.8}Sr_{0.2})_{0.95}Fe_{0.8}Ti_{0.2}O_{3-\delta}$-$Ce_{0.9}Gd_{0.1}O_{1.95}$ (LSFT-CGO), for implementation as redox-stable active layers in symmetrical and reversible SOFCs. We investigate the influence of different substrates on the VAN architecture and the mass-diffusion-driven self-assembling mechanisms leading to different structural and microstructural configurations. The nanoengineering of a redox-stable VAN film by incorporating a long-range vertical interface is proposed to enhance performance in oxidizing and reducing conditions (Figure S1, Supporting Information). Specifying the nanoscale contact between the two phases is expected to induce a synergistic enhancement of the electrochemical properties, maximizing the TPB density and optimizing the surface paths for electrochemical reactions.

2. Methods

2.1. Target preparation and film deposition

$(La_{0.8}Sr_{0.2})_{0.95}Fe_{0.8}Ti_{0.2}O_{3-\delta}$ (LSFT) and $(La_{0.8}Sr_{0.2})_{0.95}Fe_{0.8}Ti_{0.2}O_{3-\delta}$-$Ce_{0.9}Gd_{0.1}O_{1.95}$ (LSFT-CGO VAN) films were deposited by pulsed laser deposition (Surface PLD) onto $SrTiO_3$ (001) (STO), $Zr_{0.84}Y_{0.16}O_{1.92}$ (001) (YSZ) and $(LaAlO_3)_{0.3}(Sr_2TaAlO_6)_{0.7}$ (001) (LSAT) single crystals supplied by Crystec GmbH. The deposition temperature was set at 650 °C, and the oxygen pressure was maintained at 0.0066 mbar, with a target-substrate distance of 70 mm. The target material was ablated by a 248 nm KrF excimer laser (Coherent Lambda Physik GmbH) with a laser fluence of 1.2 J cm^{-2} and a repetition rate of 10 Hz.

The LSFT target was prepared by solid-state reaction using the corresponding oxides or carbonates previously calcined separately at high temperature: La_2O_3, $SrCO_3$, Fe_2O_3 and TiO_2 (Merck, purity >99.5 %). All calcined powders were mixed in an agate mortar for 15 minutes and heated at 1200 °C for 1 h. The resulting powders were grounded in ethanol media using a planetary ball mill (Pulverisette 7). The dry powders were uniaxially pressed into 25 cm diameter disks and sintered at 1400 °C for 5 h. A similar procedure was employed for the composite LSFT-CGO targets (50 % wt%), where the $Ce_{0.9}Gd_{0.1}O_{1.95}$ commercial powders (Rhodia) were mixed with the LSFT powders obtained at 1200 °C and then calcined at 1400 °C for 5 h. It is worth mentioning that both targets showed a relative density higher than 98 %.

2.2. Structural and microstructural characterization

X-ray diffraction (XRD) was employed to characterize the crystal structure of the films by performing θ–2θ, phi-scan, rocking curve and reciprocal space mapping (RSM) analyses in a Rigaku Smartlab diffractometer with a rotating Cu anode. High-resolution transmission electron microscopy (HRTEM), high-angle angular dark-field scanning transmission electron microscopy (HAADF-STEM) imaging, and Energy-dispersive X-ray spectroscopy (EDS) mappings were performed in a FEI Talos F200X. Electron-transparent lamellas for TEM were prepared using a FEI Helios Nanoslab 650 equipped with a focused ion beam (FIB). Ir/Pt coatings deposited by sputtering are needed for the preparation of the lamella that is subsequently characterized by HR-TEM, and only used for this specific purpose. These coatings are not applied to the samples for electrical characterization. Atomic force microscopy (AFM) was carried out using a Dimension Icon from Bruker.

X-ray photoelectron spectra (XPS) were collected on a Physical Electronics PHI-5700 using a MgK_α radiation. The binding energies (BE) were referenced to the adventitious C 1 s peak position at 285.0 eV (accurate ± 0.1 eV). A Shirley-type background was subtracted from the signals, and Gaussian−Lorentzian curves used to accurately determine the binding energy of the different element core levels. Fixed values for the Full Width at Half Maximum (FWHM) were employed to ensure consistent data comparison, maintaining peak splitting spacing in samples treated under both oxidizing and reducing atmospheres.

2.3. Electrical characterization

The in-plane conductivity of the samples was determined using the four-probe Van der Pauw method. Gold ink and wires were employed to connect the electrical connections to the electrochemical setup. Samples deposited onto electrically insulating LSAT substrates were specifically selected to ensure accurate electrical characterization of the films and minimize interference from the substrate conductivity. The measurements were performed in air and 5 % H_2-Ar atmospheres between 650 °C and room temperature on cooling. The conductivity was also measured as a function of the oxygen partial pressure (pO_2) to elucidate the nature of the charge carriers. For this purpose, the samples were reduced in a closed tube furnace under a 5 % H_2-Ar flow for 12 h. Afterwards, the flow was switched off, and the pO_2 was continuously monitored using a YSZ sensor while the conductivity was measured at intervals of 5 minutes during the reoxidation process. It is worth noting that each isothermal measurement is required over two days for complete reoxidation.

Additionally, the electrode polarization resistance of the films deposited on YSZ (001) was determined by impedance spectroscopy in a Solartron 1260 frequency response analyzer (FRA) in the symmetrical configuration. The frequency range was from 10^6 to 0.05 Hz, with an amplitude of 100 mV. The impedance spectra were collected on cooling between 650 and 450 °C with a stabilization time of 30 min between consecutive measurements in air, H_2 and as a function of the pO_2. Porous Au paste (Metalor) was applied onto the films to serve as a current collector and ensure uniform current distribution. The impedance data and contributions to the overall polarization resistance were analyzed by equivalent circuit models with the ZView software [44]. Additionally, distribution of relaxation times (DRT) analysis was carried out by DRT tools software to gain further insights into the different electrode processes [45].

3. Results and discussion

3.1. Influence of the substrate on the microstructural ordering of VAN films

Before investigating the functional properties of the LSFT-CGO VAN film, it is essential to conduct a thorough structural characterization. Here, we aim to analyze in detail the self-assembled process of the VAN grown on two types of substrates: perovskite (*i.e.* STO and LSAT) and fluorite substrates (*i.e.* YSZ).

The microstructure and film thickness analysis of the LSFT-CGO VAN sample on STO (001) was conducted using HAADF-STEM and EDS techniques, utilizing an electron transparent cross-sectional lamella for examination (Fig. 1). HAADF-STEM image at lower magnification revealed a long-range ordered columnar microstructure perpendicular to the substrate through the entire film thickness (approximately 100 nm). The LSFT-CGO VAN presented a dense structure without visible porosity or delamination with the substrate (see also Figure S2). The distinct contrast observed for the columns and well-defined and

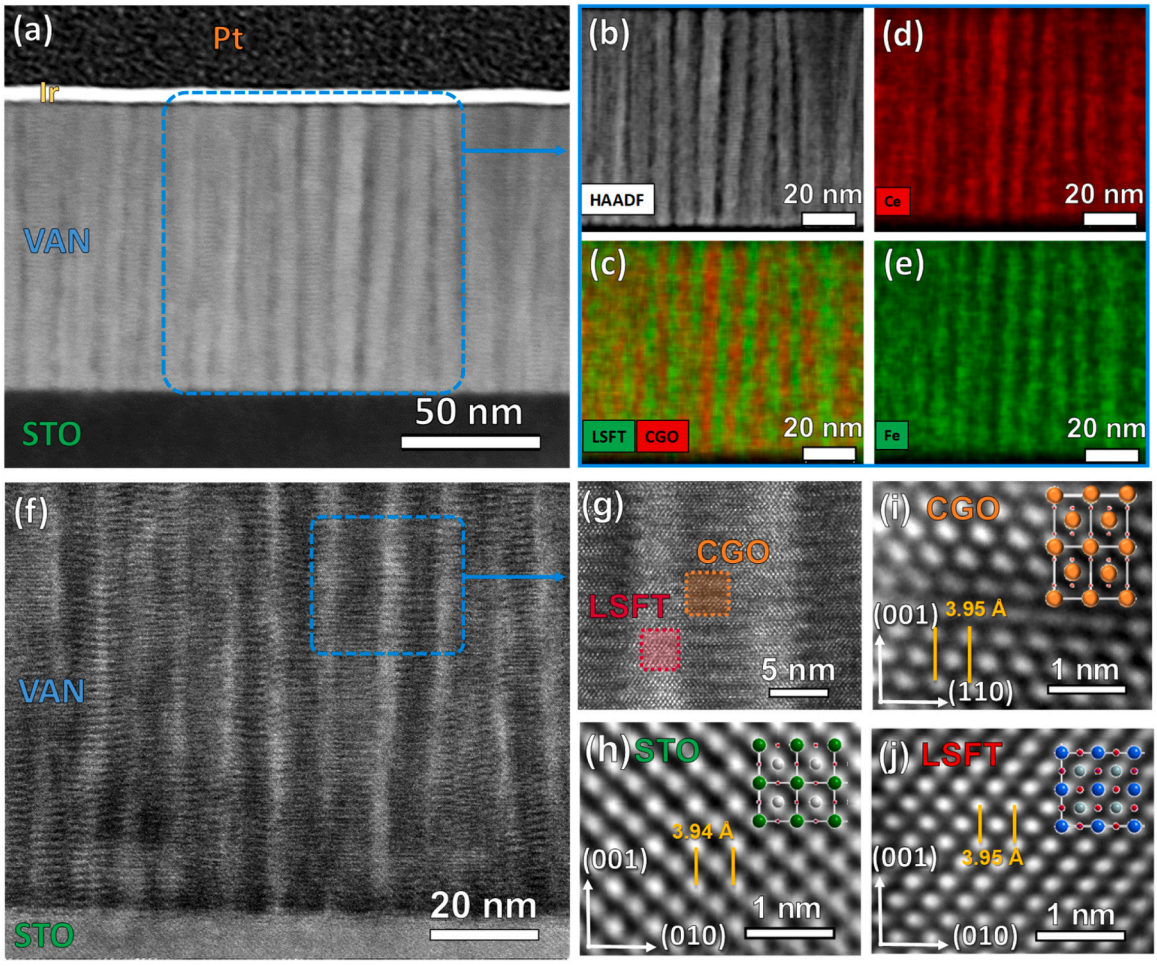

Fig. 1. (a) High magnification cross-sectional HAADF-STEM image of the LSFT-CGO VAN film deposited onto STO (001) substrate. (b) HAADF-STEM image and (c-e) EDS of a selected area of the film, unveiling the composition of the columnar microstructure. (f,g) HRTEM images of the LSFT-CGO VAN at different magnification. Atomic arrangement of (h) STO substrate, (i) CGO and (j) LSFT phases.

sharp interfaces strongly indicated the separation of the perovskite and fluorite phases within the LSFT-CGO VAN sample (Fig. 1a). The EDS mapping unveiled the formation of homogeneously distributed LSFT and CGO columns of about 5 nm width through the whole film thickness. These findings revealed the successful separation of two phases in the nanocomposite self-assembled VAN (Fig. 1b-e).

HRTEM images revealed alternating crystalline nanocolumns of 5 nm width (Fig. 1f and g). Atomic order at the HRTEM and XRD analysis confirmed the presence of perovskite LSFT and fluorite CGO phases with long vertical interfaces. The observed in-plain lattice matching relationships LSFT (001) || CGO (110) || STO (001) and out-of-plane relationships LSFT (001) || CGO (001) || STO (001) for both phases were consistent with previous perovskite-fluorite-based VANs deposited onto STO (001) [23]. In the case of the CGO component, a 45° in-plane rotation was required to minimize the lattice mismatch with the substrate. The calculated d-spacing values for both phases demonstrated a good out-of-plane relationship (Fig. 1h-j).

In a VAN structure, the spontaneous ordering of nanocolumns of two different materials is influenced by the in-plain strain, the substrate orientation and vertical interfacial strain due to the simultaneous growth of nanodomains, leading to an out-of-plane coherence [46]. The design of self-assembled thin-film nanocomposites with coherent interfaces by strain engineering offers advantages in terms of improved percolation and enhanced charge transport, surpassing those achieved through polycrystalline composite ceramics.

Furthermore, the LSFT-CGO VAN sample deposited on YSZ (001) was characterized by HAADF-STEM, EDS and HRTEM (Figure S3). Similar to the sample deposited onto STO (001) observed previously, the VAN showed a dense columnar microstructure consisting of alternating columns of LSFT and CGO phases. The substrate-film interface showed poorer phase separation due to a significant cation intermixing. However, an ordered columnar VAN architecture with coherent interfaces was attained at a distance from the interface. These findings are consistent with previous observations in the LSM-SDC VAN deposited onto YSZ (001), and they can be attributed to distinct lattice match and chemical properties of the YSZ substrate [27].

Top-view AFM images of the LSFT-CGO VAN deposited onto LSAT and YSZ (001) revealed a dense microstructure with different grain sizes and roughness for each sample (Figure S4). The VAN deposited onto LSAT showed a lower roughness (~ 2.1 nm) than the film deposited onto YSZ (~ 9.6 nm), suggesting a more disordered microstructure during the spontaneous growth of both LSFT and CGO phases onto YSZ.

XRD characterization was conducted to confirm the atomic ordering and crystal structure obtained by TEM analysis (Fig. 2). The θ-2θ XRD scans of the LSFT-CGO VAN deposited onto LSAT (001) provided evidence of a heteroepitaxial growth with a preferential (00 *l*) orientation of both the LSFT and CGO components, without any additional crystal orientations (Fig. 2a). Similar results were obtained for the LSFT-CGO VAN samples deposited on STO (001) substrates due to the similar lattice parameters between both phases (LSAT = 3.868 Å and STO = 3.905 Å). As expected, the LSFT sample exhibited epitaxial growth along the (001) orientation (see also Figure S5).

The LSFT-CGO VAN deposited onto YSZ (001) with fluorite structure (5.143 Å) showed an epitaxial growth for the CGO component with a preferred (00 *l*) orientation (Fig. 2b). However, a minor (111) reflection was also detected. On the other hand, the LSFT phase displayed a perfectly vertical orientation growth along the (110), parallel to the CGO (002). The close lattice spacing between LSFT (110) and CGO (002) induced a strong out-of-plane coherence between the two structures (Figure S6). The same behavior was previously observed for an LSM-SDC VAN deposited onto YSZ (001) [27]. Extensive research has underscored the importance of surface orientation on the catalytic activity of perovskite-oxide materials [47]. Computational studies have demonstrated that the (110) surface orientation exhibits greater catalytic activity compared to (001) for oxygen reduction in traditional SOFC cathodes such as $La_{0.5}Sr_{0.5}MnO_{3-\delta}$, $La_{0.6}Sr_{0.4}Fe_{0.8}Co_{0.2}O_{3-\delta}$ and $La_{0.6}Sr_{0.4}CoO_{3-\delta}$ [48–50].

To obtain further information about the crystal structure of the LSFT-

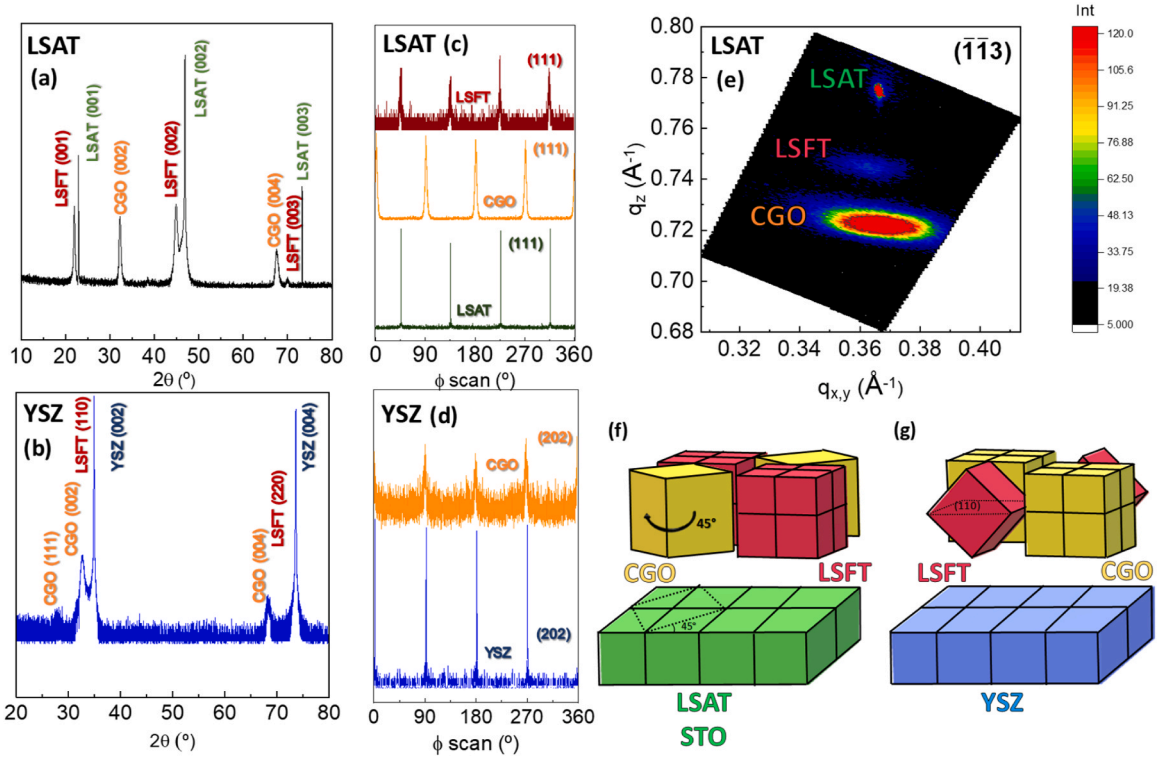

Fig. 2. θ-2θ XRD patterns of LSFT-CGO VAN deposited onto (a) LSAT (001) and (b) YSZ (001). ϕ-scan analysis of LSFT-CGO VAN deposited on (c) LSAT around the (111) direction and (d) YSZ around the (202) direction. (e) Reciprocal space map near the ($1^{-}1^{-}3$) asymmetric reflection of the LSFT-CGO VAN deposited on LSAT. Schematic representation of the heteroepitaxial growth of the samples on (f) STO and LSAT and (g) YSZ.

CGO VAN samples, ϕ-scans and reciprocal space mapping were carried out (Fig. 2c-e). The in-plane arrangement was elucidated by performing ϕ-scans on asymmetric reflections of the different components. The ϕ-scan of LSAT (111) showed four narrow peaks 90° apart in ϕ, which corresponds to a cubic perovskite structure with a [001]/[010] in-plane crystallographic growth direction. At the same time, LSFT (111) also shows four reflections at the same ϕ, consistent with a cube-on-cube growth (Fig. 2c). Interestingly, the ϕ-scan of CGO (111) presented four reflections that were shifted by 45° from LSAT (111), indicating a [110]/[010] in-plane relationship. These results confirmed the 45° cell rotation of the CGO structure onto both LSAT and STO substrates to minimize the lattice mismatch, as observed by TEM analysis.

In the case of the LSFT-CGO VAN deposited onto YSZ, the (202) ϕ-scan for both the YSZ substrate and CGO phase showed four peaks with the same ϕ displacement (Fig. 2d). However, additional reflections were not detected after the (202) ϕ-scan of the LSFT phase. A 2θ-ω rocking curve (RC) analysis was performed to clarify these results (Figure S7). In the case of the RC of LSFT (001) in the VAN on LSAT (001), a sharp and narrow peak was observed, indicating the good quality of epitaxial growth. In contrast, a wider peak is visible in the RC of CGO (002), suggesting the presence of dislocations in the film that affect the parallelism of atomic planes. This finding is common in CeO_2-based films deposited onto single crystals with perovskite structure [23,51]. In the case of the RC of LSFT (110) in the LSFT-CGO VAN onto YSZ, no extra peaks were detected, revealing the very low quality of phase order, likely due to a high concentration of crystalline defects.

Reciprocal space mapping (RSM) of LSFT-CGO VAN near the asymmetric reflection $(\overline{1}13)$ of LSAT unveiled that the LSFT phase is strained, exhibiting nearly identical in-plain lattice parameter (a = 3.889 Å) to the substrate (LSAT = 3.868 Å) (Fig. 3e). This finding confirmed the cube-on-cube growth, while a different out-of-plain lattice parameter (a = 4.062 Å) was observed. The RSM results indicated a nominal out-of-plane tensile strain of +1.7 % compared to unstrained LSFT (a = 3.919 Å), which can be associated with the in-plane lattice compression of the perovskite phase. A broad peak was obtained for the CGO phase, indicating a wide range of the in-plain lattice parameters, ranging from 5.349 to 5.571 Å. On the contrary, high coherence along the out-of-plane direction was obtained, as observed in the θ-2θ scans, which is consistent with other CeO_2-based VAN thin films [23,25,27]. The presence of the CGO spread peak near the $(\overline{1}13)$ asymmetric reflection further confirmed the 45° in-plane rotation of the fluorite phase to be accommodated onto the perovskite substrate. The similar lattice parameter of the LSFT and the substrate enables the growth of highly crystalline and perfectly aligned nanocolumns in the VAN film. It is worth mentioning that while a certain cation intermixing between the LSFT and CGO phases is plausible, it does not affect the simultaneous heteroepitaxial growth of these two phases. These findings highlight the significant influence of the substrate's crystal structure and lattice cell parameters on the nanostructure ordering. This knowledge opens up possibilities for tailoring the functional properties of the film by

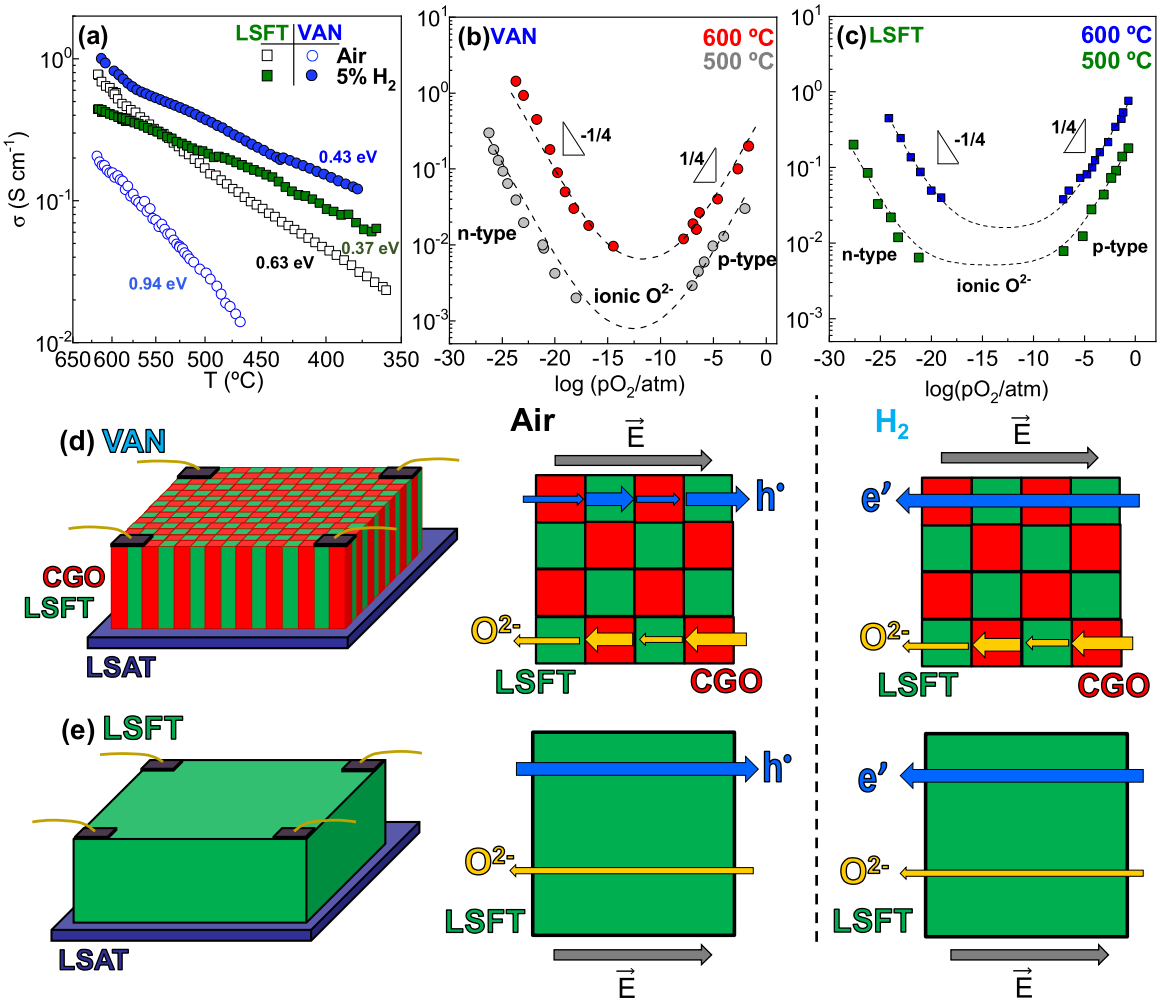

Fig. 3. (a) In-plane conductivity of the different films deposited onto LSAT (001) in air and 5 % H_2 as a function of temperature. Oxygen partial pressure (pO_2) dependence of the conductivity for (b) LSFT-CGO VAN and (c) LSFT at different temperatures. Schematic diagrams illustrating the electron and ionic conduction pathways in oxidizing and reducing atmospheres for (d) VAN and (e) LSFT films.

selecting different substrates. A schematic of the effect of the substrate is illustrated in Fig. 2f-g, which shows the crystal structure obtained for the LSFT-CGO VAN deposited onto STO and LSAT substrates (perovskite structure, Fig. 2f) in comparison with the VAN structure deposited onto YSZ (fluorite structure, Fig. 2g).

The LSFT-CGO VAN on STO (001) was annealed at 650 °C for 5 h in 5 % H_2-Ar atmosphere to investigate the redox stability. Details are reported in Figure S8. The θ-2θ XRD patterns demonstrated that the LSFT-CGO VAN remains stable in reducing conditions without forming secondary phases or other crystallographic orientations. The out-of-plane lattice parameter for the LSFT phase slightly decreased from 4.062 to 4.045 Å, indicating a partial out-of-plane cell relaxation after the reduction. A similar out-of-plain lattice parameter was observed for the CGO component. Interestingly, despite the expected increase in the out-of-plane lattice parameter due to the partial reduction of Ce^{4+} to Ce^{3+}, the dense and rigid microstructure induced by vertical strain appears to prevent significant changes in the out-of-plane lattice parameters. In this sense, significant changes in the lattice parameters under redox conditions are undesirable, as they can induce microstructural modifications that compromise the long-term cell integrity of the layers.

The chemical composition of the LSFT-CGO VAN, both as-deposited and after the reduction treatment, was characterized by XPS (Figure S9). Deconvolution of the Fe $2p_{3/2}$ core level revealed the three distinct contributions (Fe^{2+}, Fe^{3+} and Fe^{4+}) with binding energies of 709.8, 710.8 and 713.2 eV, respectively. After reduction, the Fe^{2+} band increases, indicating a partial reduction of iron, as expected. In the case of the Ce 3d signal, a reduction of Ce^{4+} to Ce^{3+} was observed on the surface. In the case of O 1 s core level, three different contributions were discerned at 529. 2, 531.0 and 532.2 eV, ascribed to lattice oxygen (O_{lat}), adsorbed oxygen (O_{ad}) and water (O_H). No significant changes were observed for the other elements after the reduction treatment. Table S1 summarizes the binding energies and composition obtained by XPS in oxidizing and reducing atmosphere.

3.2. Electrical and electrochemical characterization

The in-plain conductivity of LSFT and LSFT-CGO VAN thin films deposited onto LSAT (001) was studied using the four-probe Van der Pauw method under air and 5 % H_2-Ar atmospheres (Fig. 3a). The epitaxial LSFT exhibited conductivity values of 0.57 S cm^{-1} in air at 600 °C. Conversely, the conductivity slightly decreased to 0.40 S cm^{-1} at the same temperature in 5 % H_2-Ar due to the partial reduction of Fe^{4+} to lower oxidation states in LSFT, decreasing the density of charge carriers [42]. Consistent with previous observations, the titanium content in this sample is sufficient to prevent the phase transformation of the perovskite structure under a reducing atmosphere but insufficient to achieve high conductivity values in 5 % H_2-Ar [42]. However, increasing the titanium content would be detrimental to the electrochemical properties in oxidizing conditions, as previously reported for $La_{0.4}Sr_{0.6}Fe_{0.8-x}Ti_{0.2+x}O_{3-\delta}$ bulk ceramics [52] (x = 0–0.4) or $SrFe_{1-x}Ti_xO_{3-\delta}$ (x = 0–0.5) [53], thus limiting its application as a symmetrical functional layer.

For the LSFT-CGO VAN, the conductivity values in air reached 0.16 S cm^{-1} at 600 °C. These slightly lower conductivity values observed in air can primarily be attributed to the lower conductivity of CGO in oxidizing conditions, which is mainly an ionic conductor. However, in a 5 % H_2-Ar atmosphere, the conductivity increased to 0.82 S cm^{-1} at 600 °C, which can be attributed to the partial reduction of Ce^{4+} to Ce^{3+}, thus promoting higher electronic conductivity. Interestingly, despite the presence of alternating columns of two different phases, the dense microstructure of the VAN enables excellent in-plane percolation between the phases, resulting in enhanced conductivity.

The VAN active layers in the present study exhibit improved conducting properties compared to the single-phase film due to extended ionic and electronic pathways to the electrolyte. Additionally, they demonstrate high redox stability, making them suitable for simultaneous use as active layers for both air and fuel electrodes. Notably, the conductivity of the LSFT-CGO VAN in this work is more than one order of magnitude higher than the one obtained by LSFT-CGO composites obtained by powder ball milling, in both oxidizing and reducing conditions. At 600 °C, the LSFT-CGO VAN exhibits conductivities of 0.82 in air and 0.16 S cm^{-1} in 5 %-H_2-Ar. In contrast, polycrystalline LSFT-CGO obtained by ball milling shows significantly lower conductivities of 0.065 and 0.0017 S cm^{-1} in air and 5 %-H_2-Ar, respectively, at the same temperature. This notable improvement in conductivity for VAN films compared to traditional powder composites for SOFC has been previously reported by different authors [22,23,25]. This improvement is attributed to the nanoengineering design of the VAN, which consists of strained vertical nanocolumns that enhance transport properties.

The conductivity of both LSFT and LSFT-CGO VAN was also determined as a function of the oxygen partial pressure (pO_2) at different temperatures to elucidate the nature of the charge carriers contributing to the overall conductivity (Fig. 3b,c). All the curves were fitted according to the following equation:

$$\sigma_t = \sigma_i + \sigma_n(P_{O_2})^{-1/4} + \sigma_p(P_{O_2})^{1/4} \quad (1)$$

where σ_i, σ_n and σ_p are the ionic, n-type and p-type electronic contributions at $pO_2 = 1$ atm. As shown in Fig. 3d,e and expressed in Eq. 1., electron conduction (n-type) prevails in reducing atmospheres, while hole conduction (p-type) governs conductivity in oxidizing environments [54].

The LSFT-CGO VAN exhibited predominant n-type conductivity at low oxygen partial pressure, displaying a $(pO_2)^{-1/4}$ dependence (Fig. 3b). Furthermore, the conductivity reached a minimum value at $pO_2 \sim 10^{-13}$ atm due to the n-p transition regime. Above this pO_2, the conductivity increased with a $(pO_2)^{1/4}$ dependence attributed to a p-type contribution. This effect is mainly due to hole-conduction in agreement with the defect chemistry model in previous studies of $La_{0.9}Sr_{0.1}FeO_{3-\delta}$ and $La_{0.75}Sr_{0.25}FeO_{3-\delta}$ [55,56]. Such a behavior is typical of a mixed ionic-electronic conductor [6]. Similarly, the pO_2 curves of LSFT exhibited a comparable trend to the VAN, with both n-type and p-type contributions discernible (Fig. 3c).

However, noticeable differences were evident in both samples. In air, the ionic conductivity of LSFT-CGO VAN at intermediate pO_2 was slightly lower than that of LSFT. These results can be explained by a minor cation intermixing between LSFT and CGO phases. Indeed, previous studies have demonstrated that increasing lanthanum content in $Ce_{1-x}La_xO_{2-x/2}$ reduces the oxide-ion conductivity while maintaining the electronic contribution [57]. Most importantly, the in-plain oxide-ion mobility in the VAN may be affected by the multiple phase boundaries on the surface (nanocolumnar architecture). However, the electronic hole conductivity, mainly governed by the electronic band structure, remains relatively unaffected. It is also worth mentioning that the p-type conductivity of CGO is notably lower compared to the one observed in this work for the LSFT perovskite phase [58], which further explains these findings. In a reducing atmosphere, the LSFT-CGO VAN exhibited a higher conductivity. For example, at $pO_2 = 10^{-24}$ atm and 600 °C, the VAN exhibits a higher conductivity of 1.43 compared to 0.45 S cm^{-1} for LSFT. The observed increase in total conductivity at very low pO_2 for the VAN is assigned to the enhanced n-type conductivity of CGO in reducing environments due to the partial reduction of Ce^{4+} to Ce^{3+} [59]. The contributions of ionic and electronic conduction transport in oxidizing and reducing conditions for both samples are schematically represented in Fig. 3d and e.

Nevertheless, the out-of-plain conduction mechanisms for the VAN sample may differ from those observed in-plain due to the multiple interfaces and more favorable pathways perpendicular to the substrate (Figure S11). The high density of out-of-plane coherent transport pathways is expected to significantly enhance the conductivity of both oxide ion and electronic charge carriers [23,60], making this columnar

architecture very promising for enhancing the electrode activity for oxygen reduction and fuel oxidation reactions.

The electrode polarization resistance of LSFT and LSFT-CGO VAN on YSZ (001) was studied by electrochemical impedance spectroscopy (EIS) in a symmetrical cell configuration with Au ink serving as a current collector, i.e., Au/VAN/YSZ/VAN/Au. The measurements were performed under air and H_2 atmospheres (Fig. 4). The ohmic resistance of the electrolyte, which was similar in both cases, was subtracted to enable a more accurate comparison of the electrode response. The impedance spectra were fitted with the equivalent circuit displayed in the inset of Fig. 4a, which required three RQ elements to fit the impedance data adequately (Table S2). Symmetrical cell testing, commonly used in SOFCs, provides a better understanding of the electrocatalytic activity by isolating the performance of the electrodes.

The $LSFT_{0.2}$-CGO VAN exhibited lower polarization resistance (R_P) values in air (2.9 Ω cm^2 at 650 °C) compared to the LSFT film (6.2 Ω cm^2 at 650 °C) in all temperature range studied (Fig. 4a,b). These R_p values are comparable to those observed for other Co-free VANs recently reported in the literature, such as $La_{0.75}Sr_{0.25}Cr_{0.5}Mn_{0.5}O_{3-\delta}$-$Ce_{0.8}Sm_{0.2}O_{1.9}$ (LSCM-SDC VAN) (27.8 Ω cm^2 at 750 °C) [33] or LSM-SDC (7 Ω cm^2 at 750 ºC) [27]. Furthermore, they are similar to highly efficient thin electrodes deposited by PLD, such as $Ba_{0.5}Sr_{0.5}Co_{0.8}Fe_{0.2}O_{3-\delta}$ (BSCF) (3 Ω cm^2 at 600 °C), $Sm_{0.5}Sr_{0.5}CoO_{3-\delta}$ (SSC) (5.5 Ω cm^2 at 650 °C) or ($La_{0.6}Sr_{0.4}Co_{0.2}Fe_{0.8}O_{3-\delta}$ 20 Ω cm^2 at 650 °C) [61]. The activation energy (E_a) for the ORR decreases from 1.94 eV for LSFT to 1.75 eV for LSFT-CGO VAN.

However, the electrocatalytic performance of the LSFT-CGO VAN in air is inferior to that of Co-based VANs reported in the literature, similar to that observed for the corresponding bulk materials [37,62]. For instance, Develos-Bagarinao *et al.* investigated an LSCF-CGO vertically aligned nanocomposite prepared by PLD onto polycrystalline CGO electrolyte, achieving a polarization resistance of 0.09 Ω cm^2 at 600 °C in air [29]. Further enhancement was observed after incorporating an LSC nanoporous electrode layer on top of the dense VAN, with R_p values dropping to 0.036 Ω cm^2 at the same temperature. However, LSCF thin-films suffer from phase degradation in air atmosphere due to superficial Sr segregation after long-term annealing [63], while the VAN architecture with vertical strain engineering has demonstrated to hinder this segregation [27].

Wells et al. prepared the LSCF-SDC VAN by PLD onto YSZ single crystals, reporting R_p values of 60 Ω cm^2 at 500 °C [11]. The same nanostructured VAN electrode, when deposited onto anodized aluminium oxide (AAO) substrates and annealed in vacuum at 700 °C, showed outstanding performance with R_p values of 0.1 Ω cm^2 at 425 °C, attributed to the formation of excess oxygen vacancies in the VAN film [11]. In a different approach, Lee et al. explored a LSCF-YSZ nanoengineered electrode deposited by magnetron sputtering onto AAO [64], showing a R_p of 0.12 Ω cm^2 at 600 °C, five times lower than traditional LSCF films under similar conditions with negligible degradation over 7 h in a short-term durability test. Additionally, Yoon et al. reported a highly efficient LSC-CGO VAN prepared by PLD, with a notable R_p of 2.39 Ω cm^2 at 400 °C [65]. Enhanced ORR kinetics were also observed in heteroepitaxial VAN films composed of perovskite-Ruddlesden-Popper phases ($La_{0.8}Sr_{0.2}CoO_3$-$(La_{0.5}Sr_{0.5})_2CoO_4$), which exhibited R_p values of 10^3 Ω cm^2 at 400 °C in air atmosphere [30]. Table S3 compares the electrochemical performance in air obtained in this work with the state-of-the-art and VAN thin-films reported in literature.

In a wet H_2 atmosphere, the LSFT-CGO VAN exhibited significantly lower R_p values than the LSFT film, 75.9 and 225.4 Ω cm^2, respectively, at 650 °C (Fig. 4c,d). Although these values are considerably higher than those observed in air conditions, they are similar to those reported for the $La_{0.75}Sr_{0.25}Cr_{0.5}Mn_{0.5}O_{3-\delta}$-$Ce_{0.8}Sm_{0.2}O_{1.9}$ (LSCM-SDC VAN) (~ 80 Ω cm^2 at 630 °C) or single film of $La_{0.75}Sr_{0.25}Cr_{0.5}Mn_{0.5}O_{3-\delta}$ (~ 300 Ω cm^2 at 630 °C) [33]. The improved electrochemical properties for the hydrogen oxidation reaction (HOR) in the LSFT-CGO VAN can be attributed to the synergistic effect resulting from the nanoscale contact of both phases. For instance, Sirvent et al. reported in the LSCM-SDC VAN that nanoscale doped-CeO_2 provides active sites for fast HOR, while the LSCM phase supplies the electronic conduction pathway [33]. The activation energy for HOR in the LSFT-CGO VAN ($E_a = 1.24$ eV) was considerably lower than that observed for LSFT ($E_a = 1.74$ eV). Additionally, as expected, the activation energies for HOR were also lower than those for ORR, which can be attributed to the sluggish kinetics of the ORR.

Therefore, the electrode performance for ORR and HOR differs because the electrochemical reactions involved in both processes are different. To support our experimental results, previous studies on polycrystalline (La,Sr)(Fe,Ti)O_3 electrodes have consistently reported

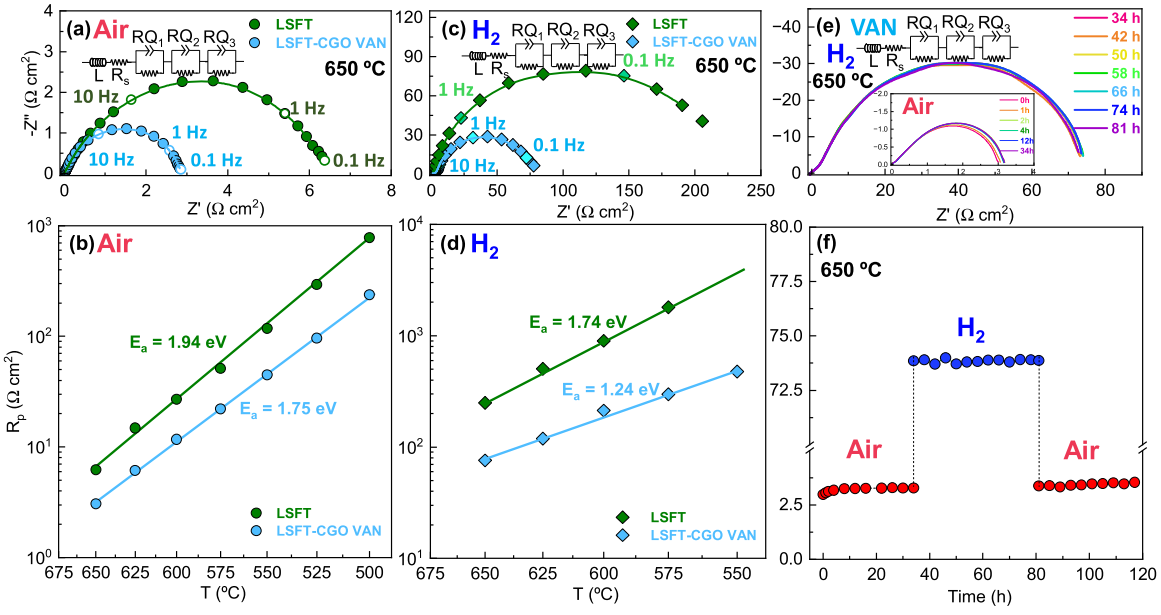

Fig. 4. (a) Impedance spectra of LSFT film and LSFT-CGO VAN at 650 °C in air and (b) Arrhenius plots of the R_P as a function of the temperature. (c) Impedance spectra of LSFT and LSFT-CGO VAN at 650 °C in H_2 and (d) Arrhenius plot of the R_P as a function of the temperature. (e) Impedance spectra in H_2 and air (inset) at different times, and (f) R_P values of the stability test performed at 650 °C as a function of the time for LSFT-CGO VAN.

considerably lower R_p in air compared to H_2 [38,42,66], aligning with the lower performance of the VAN in H_2 compared to air in this study. Nevertheless, the performance of the VAN in H_2 is nearly three times higher than that of the LSFT film under the same conditions, attributed to the nanoscale contact between LSFT and CGO phases in the VAN and the increased TPB length for electrochemical reactions.

The enhancement in electrocatalytic activity in the VAN active layer, as determined by impedance spectroscopy, is primarily attributed to its hierarchical columnar microstructure with multiple vertical interphases, which substantially enlarges the TPB for the electrochemical reactions on the film surface, compared to single-phase films. This improvement is more attributable to the hierarchical columnar microstructure obtained by nanoengineering than to variations in conductivity. This columnar architecture ensures fast oxygen reduction and hydrogen oxidation kinetics by providing more active sites and reducing the activation energy. The microstructural architecture of the VAN, composed of strained nanocolumns, provides coherent and more selective paths for ion transport, which are not available in a dense film formed by a random mixing of two phases. Additionally, the favorable out-of-plane columnar architecture facilitates fast diffusion through the vertical boundaries for oxide-ion transport, in contrast to epitaxial LSFT, where the ionic pathway provided by the CGO is unavailable.

In thin films and electrode layers, microscopic features such as porosity, morphology, and roughness significantly impact the electrochemical activity. However, accounting for these morphological differences can be challenging, leading to standardized normalization by the electrode area (Ω cm^2) in both literature and commercial devices. For example, a "poorly fabricated" VAN film may exhibit a lower R_p than a "coherently ordered" VAN due to partial phase mixing that increases phase boundary density and/or higher porosity. These microstructural differences may hinder a direct comparison with previous VANs reported in literature. Nonetheless, an ordered VAN with a strained nanocolumnar architecture, like the one presented in this work, offers coherent and more selective ion transport pathways, which are not available in a dense film formed by a random phase mixing. In the case of the LSFT-CGO VAN, HR-TEM and AFM analyses revealed that the film is dense, with a roughness in the nanometer scale, indicating a low surface area comparable to other VANs reported in literature such as LSM-SDC, LSCM-SDC or STO-SDC [23,27,33]. Tailoring the microstructure and porosity of the VAN is expected to enhance the electrochemical performance further.

Despite the relatively high R_p values obtained in this work, it is essential to note that the active layers obtained by PLD are fully dense, resulting in a relatively low surface area for oxygen reduction or hydrogen oxidation reactions. Consequently, the polarisation resistance (R_p) is higher than that of a porous electrode, and a direct comparison with conventional thick porous electrodes is not straightforward and requires careful contextualisation. In the literature, dense layers consistently exhibit relatively high R_p values. For instance, J. Maier et col. studied various traditional SOFC cathodes deposited by PLD, such as $La_{0.6}Sr_{0.4}Co_{0.8}Fe_{0.2}O_{3-\delta}$ (LSFC) or $Sm_{0.5}Sr_{0.5}CoO_{3-\delta}$ (SSC), reporting R_p values of 20 and 6 Ω cm^2, respectively, at 650 °C in air [61]. In contrast, porous electrodes of the same composition, deposited by traditional screen-printing, showed R_p values almost two orders of magnitude lower: LSCF (0.5 Ω cm^2 at 650 °C [67]) and SSC (0.28 Ω cm^2 at 650 °C [68]). On the other hand, when comparing our results with those of other dense thin films, we find that we achieved remarkable performance for the VANs. Incorporating a porous thick electrode on top of the VAN active layer is expected to improve efficiency considerably [7,27,29].

The redox stability of the LSFT-CGO VAN was tested over 120 h at 650 °C (Fig. 4e,f). The LSFT-CGO VAN exhibited a minor initial performance decrease, followed by a very low degradation over time under oxidizing and reducing conditions during cycling. This remarkable redox stability is crucial for its application as a functional layer in symmetrical and reversible SOFCs. Moreover, previous studies have also demonstrated that nano strain engineering in vertically aligned nanocomposites can improve the thermal stability in air by effectively suppressing the Sr migration to the film surface [27,29,33].

To elucidate the rate limiting steps for the oxygen reduction reactions (ORR), impedance spectra were collected at different oxygen partial pressures (pO_2). Each elementary process exhibits a different dependency on pO_2, and the relationship between the resistance of each process and pO_2 is expressed by the following equation: $R \propto (pO_2)^m$,

where the exponent m provides insights into the nature of the sub-reaction in the ORR.

DRT deconvolution of the impedance spectra as function of the pO_2 reveals three electrode processes (Fig. 5c). The high frequency (HF) response, centered at ~10^4 Hz, shows negligible dependency on the oxygen partial pressure, and is assigned to oxide-ion transport at the VAN/electrolyte interphase ($O^x_{o,\ VAN} \rightarrow O^x_{o,\ electrolyte}$) (Fig. 5d) [69,70]. The intermediate frequency electrode response (IF), which is the main contribution to the overall polarization resistance, exhibited a pO_2 dependence with a reaction order of $m \sim 0.25$. This is associated with the charge transfer process at the electrode surface ($O_{ads} + 2e^- + V_o^{\cdot} \rightarrow O_o^x$) [71]. Additionally, this process shifts to higher frequencies as pO_2 increases, indicating a lower relaxation time and faster electrode kinetics. A third contribution at low frequency, labelled as LF and centered at 1 Hz, becomes discernible at low pO_2. This contribution exhibited a strong dependence on the pO_2, with a $m \sim 0.80$, is associated with adsorption of molecular oxygen on surface ($O_{2,(g)} \rightarrow O_{2,ad}$) [67]. Table S4 summarizes the different rate-determining steps and the corresponding reactions order. Figure S12 illustrates the rate-determining in the VAN for the ORR.

Our study presents extensive research on the new concept of redox-stable VAN active layers for energy conversion devices, demonstrating improved electrochemical performance under oxidizing and reducing conditions compared to single-phase films. This enhancement is due to the extended ionic and electronic pathways for electrochemical reactions, which results from the hierarchical microstructure of the VAN. Future work on implementing redox-stable VAN active layers and porous electrodes is expected to enhance the performance in single-cell configuration.

4. Conclusions

Novel functional layers based on $(La_{0.8}Sr_{0.2})_{0.95}Fe_{0.8}Ti_{0.2}O_{3-\delta}$-$Ce_{0.9}Gd_{0.1}O_{1.95}$, (LSFT-CGO) comprising redox-stable vertically aligned nanostructures (VAN), prepared by pulsed laser deposition, were investigated for their potential application in symmetrical and reversible solid oxide fuel cells (SOFCs). Structural and microstructural characterization has revealed the influence of the substrate composition on the thin film architecture and columnar microstructure growth. A clear phase separation was observed in the VAN deposited onto STO substrate throughout the entire 100 nm film thickness. In contrast, when the VAN was deposited onto YSZ substrates, a minor cation intermixing was observed near to the substrate-film interface before the formation of the ordered columnar architecture. The self-assembled process resulted in the formation of long-range nanocolumns of perovskite and fluorite phases, which facilitated favorable out-of-plane transport pathways, enabling fast oxide-ion transport from the TPB to the electrolyte.

The VAN exhibited in-plane conductivity values under reducing conditions of 0.82 S cm^{-1} at 600 °C, which were higher than those observed for LSFT at the same temperature (0.40 S cm^{-1}). This improvement was attributed to the higher n-type electronic conduction of the CGO component in an H_2 atmosphere. However, under oxidizing conditions, the conductivity of the VAN decreased to 0.16 S cm^{-1} at 600 °C, which was lower than the epitaxial LSFT (0.57 S cm^{-1}), attributed to the lower p-type conductivity of the CGO compared to the perovskite component. Nevertheless, the nanocolumnar architecture, with multiple phase boundaries at the surface, may negatively affect the in-plain oxide-ion transport. In contrast, the out-of-plane configuration with

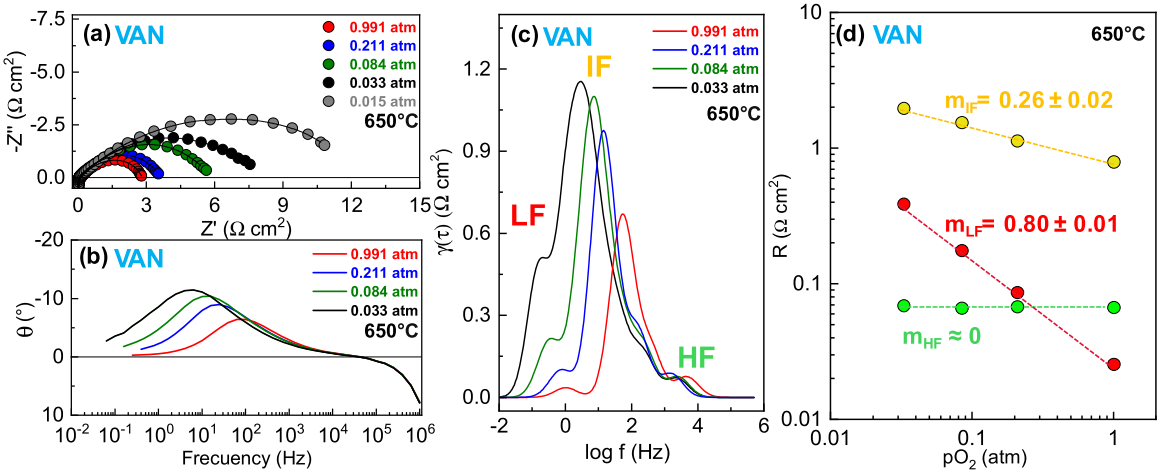

Fig. 5. (a) Impedance spectra, (b) bode plot and (c) DRT analysis of LSFT-CGO VAN at 650 °C as a function of the pO_2. (d) Dependence of the different electrode resistances as function of the pO_2.

coherent conducting pathways perpendicular to the surface is favorable and desirable in real SOFC devices. Compared to single-phase active layers, the intimate nanoscale contact between LSFT perovskite and CGO fluorite phases maximizes the TPB length for electrochemical reactions.

Moreover, we demonstrate that the VANs possess a tunable regime of strained interfaces, which accelerate the redox process and enhances the reactivity with the environment. The synergistic combination of both phases, with excellent phase alternation, significantly increased the electrode performance in oxidizing and reducing conditions. Specifically, the VAN exhibited R_p values of 2.9 and 75.9 Ω cm^2 at 650 °C in air and H_2, respectively, compared to 6.2 and 225.4 Ω cm^2 for LSFT film. Moreover, the VAN showed high stability over time and during redox cycling. The remarkable performance and redox stability of the Co-free LSFT-CGO VAN films with vertically aligned architecture make them strong candidates for symmetrical and reversible SOFCs. Future research exploring alternative dopant strategies could further enhance the electrochemical activity in air, addressing the current limitations compared to Co-based VANs films. However, Co-based materials are not stable under a reducing atmosphere, which is a critical factor for applying reversible and symmetrical SOFCs, which is the core context of our study. In addition, single cell testing with a porous electrode on top of the VAN active layer is expected to enhance the electrochemical performance of reversible and symmetrical SOFCs. The nanoengineering design of a self-assembled redox-stable VAN with a hierarchical columnar architecture, demonstrating improved conductivity and electrochemical properties, represents a decisive advancement in integrating highly active symmetrical thin functional oxides into energy conversion devices.

CRediT authorship contribution statement

Javier Zamudio-García: Writing – original draft, Investigation, Formal analysis, Data curation, Conceptualization. **Francesco Chiabrera:** Writing – review & editing, Validation, Methodology, Investigation. **Enrique R. Losilla:** Writing – review & editing, Validation. **David Marrero-López:** Writing – review & editing, Visualization, Funding acquisition. **Vincenzo Esposito:** Writing – review & editing, Project administration, Funding acquisition, Formal analysis, Conceptualization.

Declaration of Competing Interest

The authors declare that they have no known competing financial interests or personal relationships that could have appeared to influence the work reported in this paper.

Data availability

Data will be made available on request.

Acknowledgements

The authors acknowledge the projects PID2021-126009OB-I00 and TED2021-129836B-I00, funded by MCIN/AEI/10.13039/501100011033 and by "ERDF A way of making Europe", by the European Union and Independent Research Fund Denmark (Grant No. 9041-00034B and 1032-00261B) research grants. JZG thanks the Ministerio de Ciencia, Innovación y Universidades for his FPU grant (FPU17/02621) and his Postdoctoral contact at DTU.

Appendix A. Supporting information

Supplementary data associated with this article can be found in the online version at doi:10.1016/j.nanoen.2024.110293.

References

[1] T.M. Gür, Review of electrical energy storage technologies, materials and systems: challenges and prospects for large-scale grid storage, Energy Environ. Sci. 11 (2018) 2696–2767, https://doi.org/10.1039/c8ee01419a.
[2] N. Mahato, A. Banerjee, A. Gupta, S. Omar, K. Balani, Progress in material selection for solid oxide fuel cell technology: a review, Prog. Mater. Sci. 72 (2015) 141–337, https://doi.org/10.1016/j.pmatsci.2015.01.001.
[3] S. Zarabi Golkhatmi, M.I. Asghar, P.D. Lund, A review on solid oxide fuel cell durability: latest progress, mechanisms, and study tools, Renew. Sustain. Energy Rev. 161 (2022), https://doi.org/10.1016/j.rser.2022.112339.
[4] M. Singh, D. Zappa, E. Comini, Solid oxide fuel cell: decade of progress, future perspectives and challenges, Int. J. Hydrog. Energy 46 (2021) 27643–27674, https://doi.org/10.1016/j.ijhydene.2021.06.020.
[5] M. Acosta, F. Baiutti, A. Tarancón, J.L. MacManus-Driscoll, Nanostructured materials and interfaces for advanced ionic electronic conducting oxides, Adv. Mater. Interfaces 6 (2019), https://doi.org/10.1002/admi.201900462.
[6] J. Zhang, S. Ricote, P.V. Hendriksen, Y. Chen, Advanced materials for thin-film solid oxide fuel cells: recent progress and challenges in boosting the device performance at low temperatures, Adv. Funct. Mater. 32 (2022), https://doi.org/10.1002/adfm.202111205.
[7] M. Machado, F. Baiutti, L. Bernadet, A. Morata, M. Nuñez, J.P. Ouweltjes, F. C. Fonseca, M. Torrell, A. Tarancón, Functional thin films as cathode/electrolyte interlayers: a strategy to enhance the performance and durability of solid oxide fuel cells, J. Mater. Chem. A Mater. 10 (2022) 17317–17325, https://doi.org/10.1039/d2ta03641j.
[8] J. Zamudio-García, L. Caizán-Juanarena, J.M. Porras-Vázquez, E.R. Losilla, D. Marrero-López, Boosting the performance of $La_{0.8}Sr_{0.2}MnO_{3-\delta}$ electrodes by the incorporation of nanocomposite active layers, Adv. Mater. Interfaces 9 (2022), https://doi.org/10.1002/admi.202200702.

[9] T. Wang, X. Shi, R. Peng, G. Dong, H. Liu, B. Chen, M. Guan, Y. Zhao, B. Peng, C. Zhou, S. Yang, W. Qu, Y. Zhang, Z. Zhou, X. Ding, H. Wu, H. Huang, M. Liu, Giant energy storage of flexible composites by embedding superparaelectric single-crystal membranes, Nano Energy 113 (2023), https://doi.org/10.1016/j.nanoen.2023.108511.

[10] H. Tan, A. Quintana, N. Dix, S. Estandía, J. Sort, F. Sánchez, I. Fina, Photovoltaic-driven dual optical writing and non-destructive voltage-less reading of polarization in ferroelectric $Hf_{0.5}Zr_{0.5}O_2$ for energy efficient memory devices, Nano Energy 123 (2024), https://doi.org/10.1016/j.nanoen.2024.109384.

[11] M.P. Wells, A.J. Lovett, Y. Zhang, Z. Shang, K. Kreka, B. Bakhit, H. Wang, A. Tarancón, J.L. MacManus-Driscoll, Pathway to high performance, low temperature thin-film solid oxide cells grown on porous anodised aluminium oxide, Nano Energy 119 (2024), https://doi.org/10.1016/j.nanoen.2023.109049.

[12] S. Choi, C.J. Kucharczyk, Y. Liang, X. Zhang, I. Takeuchi, H.Il Ji, S.M. Haile, Exceptional power density and stability at intermediate temperatures in protonic ceramic fuel cells, Nat. Energy 3 (2018) 202–210, https://doi.org/10.1038/s41560-017-0085-9.

[13] S. Choi, T.C. Davenport, S.M. Haile, Protonic ceramic electrochemical cells for hydrogen production and electricity generation: exceptional reversibility, stability, and demonstrated faradaic efficiency, Energy Environ. Sci. 12 (2019) 206–215, https://doi.org/10.1039/c8ee02865f.

[14] A.J. Lovett, M.P. Wells, Z. He, J. Lu, H. Wang, J.L. Macmanus-Driscoll, High ionic conductivity in fluorite δ-bismuth oxide-based vertically aligned nanocomposite thin films, J. Mater. Chem. A Mater. 10 (2022) 3478–3484, https://doi.org/10.1039/d1ta07308g.

[15] M.P. Wells, A.J. Lovett, T. Chalklen, F. Baiutti, A. Tarancón, X. Wang, J. Ding, H. Wang, S. Kar-Narayan, M. Acosta, J.L. Macmanus-Driscoll, Route to high-performance micro-solid oxide fuel cells on metallic substrates, ACS Appl. Mater. Interfaces 13 (2021) 4117–4125, https://doi.org/10.1021/acsami.0c15368.

[16] A.J. Abd Aziz, N.A. Baharuddin, M.R. Somalu, A. Muchtar, Review of composite cathodes for intermediate-temperature solid oxide fuel cell applications, Ceram. Int. 46 (2020) 23314–23325, https://doi.org/10.1016/j.ceramint.2020.06.176.

[17] P.A. Connor, X. Yue, C.D. Savaniu, R. Price, G. Triantafyllou, M. Cassidy, G. Kerherve, D.J. Payne, R.C. Maher, L.F. Cohen, R.I. Tomov, B.A. Glowacki, R. V. Kumar, J.T.S. Irvine, Tailoring SOFC electrode microstructures for improved performance, Adv. Energy Mater. 8 (2018) 1–20, https://doi.org/10.1002/aenm.201800120.

[18] X. Sun, J.L. MacManus-Driscoll, H. Wang, Spontaneous ordering of oxide-oxide epitaxial vertically aligned nanocomposite thin films, Annu Rev. Mater. Res. 50 (2020) 229–253, https://doi.org/10.1146/annurev-matsci-091719-112806.

[19] J. Huang, W. Li, H. Yang, J.L. MacManus-Driscoll, Tailoring physical functionalities of complex oxides by vertically aligned nanocomposite thin-film design, MRS Bull. 46 (2021) 159–167, https://doi.org/10.1557/s43577-021-00028-0.

[20] Z. Wang, Y. Li, R. Viswan, B. Hu, V.G. Harris, J. Li, D. Viehland, Engineered magnetic shape anisotropy in $BiFeO_3$-$CoFe_2O_4$ self-assembled thin films, ACS Nano 7 (2013) 3447–3456, https://doi.org/10.1021/nn4003506.

[21] S.A. Harrington, J. Zhai, S. Denev, V. Gopalan, H. Wang, Z. Bi, S.A.T. Redfern, S. H. Baek, C.W. Bark, C.B. Eom, Q. Jia, M.E. Vickers, J.L. MacManus-Driscoll, Thick lead-free ferroelectric films with high Curie temperatures through nanocomposite-induced strain, Nat. Nanotechnol. 6 (2011) 491–495, https://doi.org/10.1038/nnano.2011.98.

[22] S. Lee, J.L. MacManus-Driscoll, Research update: fast and tunable nanoionics in vertically aligned nanostructured films, APL Mater. 5 (2017) 042304, https://doi.org/10.1063/1.4978550.

[23] S.M. Yang, S. Lee, J. Jian, W. Zhang, P. Lu, Q. Jia, H. Wang, T. Won Noh, S. V. Kalinin, J.L. MacManus-Driscoll, Strongly enhanced oxygen ion transport through samarium-doped CeO2 nanopillars in nanocomposite films, Nat. Commun. 6 (2015) 1–8, https://doi.org/10.1038/ncomms9588.

[24] C. Zhao, Y. Li, W. Zhang, Y. Zheng, X. Lou, B. Yu, J. Chen, Y. Chen, M. Liu, J. Wang, Heterointerface engineering for enhancing the electrochemical performance of solid oxide cells, Energy Environ. Sci. 13 (2020) 53–85, https://doi.org/10.1039/c9ee02230a.

[25] A. Chen, Q. Su, H. Han, E. Enriquez, Q. Jia, Metal oxide nanocomposites: a perspective from strain, defect, and interface, Adv. Mater. 31 (2019), https://doi.org/10.1002/adma.201803241.

[26] M. Xu, J. Yu, Y. Song, R. Ran, W. Wang, Z. Shao, Advances in ceramic thin films fabricated by pulsed laser deposition for intermediate-temperature solid oxide fuel cells, Energy Fuels 34 (2020) 10568–10582, https://doi.org/10.1021/acs.energyfuels.0c02338.

[27] F. Baiutti, F. Chiabrera, M. Acosta, D. Diercks, D. Parfitt, J. Santiso, X. Wang, A. Cavallaro, A. Morata, H. Wang, A. Chroneos, J. MacManus-Driscoll, A. Tarancon, A high-entropy manganite in an ordered nanocomposite for long-term application in solid oxide cells, Nat. Commun. 12 (2021), https://doi.org/10.1038/s41467-021-22916-4.

[28] J. Yoon, S. Cho, J.H. Kim, J. Lee, Z. Bi, A. Serquis, X. Zhang, A. Manthiram, H. Wang, Vertically aligned nanocomposite thin films as a cathode/electrolyte interface layer for thin-film solid oxide fuel cells, Adv. Funct. Mater. 19 (2009) 3868–3873, https://doi.org/10.1002/adfm.200901338.

[29] K. Develos-Bagarinao, T. Ishiyama, H. Kishimoto, H. Shimada, K. Yamaji, Nanoengineering of cathode layers for solid oxide fuel cells to achieve superior power densities, Nat. Commun. 12 (2021) 1–12, https://doi.org/10.1038/s41467-021-24255-w.

[30] W. Ma, J.J. Kim, N. Tsvetkov, T. Daio, Y. Kuru, Z. Cai, Y. Chen, K. Sasaki, H. L. Tuller, B. Yildiz, Vertically aligned nanocomposite $La_{0.8}Sr_{0.2}CoO_3$/$(La_{0.5}Sr_{0.5})_2CoO_4$ cathodes-electronic structure, surface chemistry and oxygen reduction kinetics, J. Mater. Chem. A 3 (2015) 207–219, https://doi.org/10.1039/c4ta04993d.

[31] S. Cho, Y.N. Kim, J. Lee, A. Manthiram, H. Wang, Microstructure and electrochemical properties of $PrBaCo_2O_{5+\delta}$/$Ce_{0.9}Gd_{0.1}O_{1.95}$ vertically aligned nanocomposite thin film as interlayer for thin film solid oxide fuel cells, Electro Acta 62 (2012) 147–152, https://doi.org/10.1016/j.electacta.2011.12.008.

[32] B.S. Kang, J. Matsuda, Y.W. Ju, H.H. Kim, T. Ishihara, Nano strain induced double columnar oxide as highly active oxygen-dissociation electrode for Ni-Fe metal supported solid oxide fuel cells, Nano Energy 56 (2019) 382–390, https://doi.org/10.1016/j.nanoen.2018.11.074.

[33] J.D.D. Sirvent, A. Carmona, L. Rapenne, F. Chiabrera, A. Morata, M. Burriel, F. Baiutti, A. Tarancón, Nanostructured $La_{0.75}Sr_{0.25}Cr_{0.5}Mn_{0.5}O_3$-$Ce_{0.8}Sm_{0.2}O_2$ heterointerfaces as All-ceramic functional layers for solid oxide fuel cell applications, ACS Appl. Mater. Interfaces 14 (2022) 42178–42187, https://doi.org/10.1021/acsami.2c14044.

[34] P. Boldrin, E. Ruiz-Trejo, J. Mermelstein, J.M. Bermúdez Menéndez, T. RamÍrez, Reina, N.P. Brandon, Strategies for carbon and sulfur tolerant solid oxide fuel cell materials, incorporating lessons from heterogeneous catalysis, Chem. Rev. 116 (2016) 13633–13684, https://doi.org/10.1021/acs.chemrev.6b00284.

[35] C. Graves, S.D. Ebbesen, S.H. Jensen, S.B. Simonsen, M.B. Mogensen, Eliminating degradation in solid oxide electrochemical cells by reversible operation, Nat. Mater. 14 (2015) 239–244, https://doi.org/10.1038/nmat4165.

[36] J. Zamudio-García, L. Caizán-Juanarena, J.M. Porras-Vázquez, E.R. Losilla, D. Marrero-López, A review on recent advances and trends in symmetrical electrodes for solid oxide cells, J. Power Sources 520 (2022), https://doi.org/10.1016/j.jpowsour.2021.230852.

[37] N.A. Baharuddin, A. Muchtar, M.R. Somalu, Short review on cobalt-free cathodes for solid oxide fuel cells, Int. J. Hydrog. Energy 42 (2017) 9149–9155, https://doi.org/10.1016/j.ijhydene.2016.04.097.

[38] Y. Hou, L. Wang, L. Bian, Y. Wang, K.C. Chou, Excellent electrochemical performance of $La_{0.3}Sr_{0.7}Fe_{0.9}Ti_{0.1}O_{3-\delta}$ as a symmetric electrode for solid oxide cells, ACS Appl. Mater. Interfaces 13 (2021) 22381–22390, https://doi.org/10.1021/acsami.1c02856.

[39] Z. Cao, Y. Zhang, J. Miao, Z. Wang, Z. Lü, Y. Sui, X. Huang, W. Jiang, Titanium-substituted lanthanum strontium ferrite as a novel electrode material for symmetrical solid oxide fuel cell, Int J. Hydrog. Energy 40 (2015) 16572–16577, https://doi.org/10.1016/j.ijhydene.2015.10.010.

[40] J. Xu, X. Zhou, X. Dong, L. Pan, K. Sun, Catalytic activity of infiltrated $La_{0.3}Sr_{0.7}Ti_{0.3}Fe_{0.7}O_{3-\delta}$–$CeO_2$ as a composite SOFC anode material for H2 and CO oxidation, Int. J. Hydrog. Energy 42 (2017) 15632–15640, https://doi.org/10.1016/j.ijhydene.2017.05.016.

[41] J. Xu, X. Zhou, J. Cheng, L. Pan, M. Wu, X. Dong, K. Sun, Electrochemical performance of highly active ceramic symmetrical electrode $La_{0.3}Sr_{0.7}Ti_{0.3}Fe_{0.7}O_{3-\delta}$–$CeO_2$ for reversible solid oxide cells, Electro Acta 257 (2017) 64–72, https://doi.org/10.1016/j.electacta.2017.10.061.

[42] J. Zamudio-García, J.M. Porras-Vázquez, E.R. Losilla, D. Marrero-López, Enhancing the electrochemical performance in symmetrical solid oxide cells through nanoengineered redox-stable electrodes with exsolved nanoparticles, ACS Appl. Mater. Interfaces (2023), https://doi.org/10.1021/acsami.3c13641.

[43] Y. Hou, L. Wang, L. Bian, Y. Wang, K. chih Chou, R.V. Kumar, High-performance $La_{0.3}Sr_{0.7}Fe_{0.9}Ti_{0.1}O_{3-\delta}$ as fuel electrode for directly electrolyzing CO2 in solid oxide electrolysis cells, Electro Acta 342 (2020), https://doi.org/10.1016/j.electacta.2020.136026.

[44] D. Johnson, ZView, A Software Program for IES Analysis, Version 2.8. Scribner Associates, Inc., Southern Pines, NC (2002), (n.d.).

[45] T.H. Wan, M. Saccoccio, C. Chen, F. Ciucci, Influence of the discretization methods on the distribution of relaxation times deconvolution: implementing radial basis functions with DRTtools, Electro Acta 184 (2015) 483–499, https://doi.org/10.1016/j.electacta.2015.09.097.

[46] J. Huang, J.L. MacManus-Driscoll, H. Wang, New epitaxy paradigm in epitaxial self-assembled oxide vertically aligned nanocomposite thin films, J. Mater. Res. 32 (2017) 4054–4066, https://doi.org/10.1557/jmr.2017.281.

[47] R. Gao, A. Fernandez, T. Chakraborty, A. Luo, D. Pesquera, S. Das, G. Velarde, V. Thoréton, J. Kilner, T. Ishihara, S. Nemšák, E.J. Crumlin, E. Ertekin, L. W. Martin, Correlating surface crystal orientation and gas kinetics in perovskite oxide electrodes, Adv. Mater. 33 (2021), https://doi.org/10.1002/adma.202100977.

[48] Y.M. Choi, M.C. Lin, M. Liu, Computational study on the catalytic mechanism of oxygen reduction on $La_{0.5}Sr_{0.5}MnO_3$ in solid oxide fuel cells, Angew. Chem. Int. Ed. 46 (2007) 7214–7219, https://doi.org/10.1002/anie.200700411.

[49] Z. Wang, R. Peng, W. Zhang, X. Wu, C. Xia, Y. Lu, Oxygen reduction and transport on the $La_{1-x}Sr_xCo_{1-y}Fe_yO_{3-\delta}$ cathode in solid oxide fuel cells: a first-principles study, J. Mater. Chem. A Mater. 1 (2013) 12932–12940, https://doi.org/10.1039/c3ta11554b.

[50] M. Komo, A. Hagiwara, S. Taminato, M. Hirayama, R. Kanno, Oxygen evolution and reduction reactions on $La_{0.8}Sr_{0.2}CoO_3$ (001), (110), and (111) surfaces in an alkaline solution, Electrochemistry 80 (2012) 834–838, https://doi.org/10.5796/electrochemistry.80.834.

[51] S. Cho, C. Yun, S. Tappertzhofen, A. Kursumovic, S. Lee, P. Lu, Q. Jia, M. Fan, J. Jian, H. Wang, S. Hofmann, J.L. MacManus-Driscoll, Self-assembled oxide films with tailored nanoscale ionic and electronic channels for controlled resistive switching, Nat. Commun. 7 (2016), https://doi.org/10.1038/ncomms12373.

[52] D.P. Fagg, V.V. Kharton, J.R. Frade, A.A.L. Ferreira, Stability and mixed ionic-electronic conductivity of (Sr,La)(Ti,Fe)O3-d perovskites, n.d. www.elsevier.com/locate/ssi.

[53] N.A. Baharuddin, N.A. Mohd Nazrul Aman, A. Muchtar, M.R. Somalu, A. Abdul Samat, M.I. Aznam, Structural, morphological, and electrochemical behavior of titanium-doped $SrFe_{1-x}Ti_xO_{3-\delta}$ (x = 0.1–0.5)perovskite as a cobalt-free solid oxide fuel cell cathode, Ceram. Int. 45 (2019) 12903–12909, https://doi.org/10.1016/j.ceramint.2019.03.216.

[54] C.B. Gopal, S.M. Haile, An electrical conductivity relaxation study of oxygen transport in samarium doped ceria, J. Mater. Chem. A 2 (2014) 2405–2417, https://doi.org/10.1039/c3ta13404k.

[55] I. Wærnhus, T. Grande, K. Wiik, Surface exchange of oxygen in La1-xSrxFeO3-δ (x = 0, 0.1), Top. Catal. 54 (2011) 1009–1015, https://doi.org/10.1007/s11244-011-9712-z.

[56] J. Mizusaki, T. Sasamoto, W.R. Cannon, H.K. Bowen, Electronic conductivity, seebeck coefficient, and defect structure of $LaFeO_3$, J. Am. Ceram. Soc. 65 (1982) 363–368, https://doi.org/10.1111/j.1151-2916.1982.tb10485.x.

[57] J. Zamudio-García, J.M. Porras-Vázquez, J. Canales-Vázquez, A. Cabeza, E. R. Losilla, D. Marrero-López, Relationship between the structure and transport properties in the $Ce_{1-x}La_xO_{2-x/2}$ system, Inorg. Chem. 58 (2019) 9368–9377, https://doi.org/10.1021/acs.inorgchem.9b01104.

[58] A. Shaur, M. Drazkowski, S. Zhu, B. Boukamp, H.J.M. Bouwmeester, A single-phase gadolinium-doped ceria cathode for highly efficient CO_2 electrolysis, J. Mater. Chem. A Mater. 11 (2023) 25020–25030, https://doi.org/10.1039/d3ta03977c.

[59] R. Schmitt, A. Nenning, O. Kraynis, R. Korobko, A.I. Frenkel, I. Lubomirsky, S. M. Haile, J.L.M. Rupp, A review of defect structure and chemistry in ceria and its solid solutions, Chem. Soc. Rev. 49 (2020) 554–592, https://doi.org/10.1039/c9cs00588a.

[60] Q. Su, D. Yoon, A. Chen, F. Khatkhatay, A. Manthiram, H. Wang, Vertically aligned nanocomposite electrolytes with superior out-of-plane ionic conductivity for solid oxide fuel cells, J. Power Sources 242 (2013) 455–463, https://doi.org/10.1016/j.jpowsour.2013.05.137.

[61] F.S. Baumann, J. Fleig, G. Cristiani, B. Stuhlhofer, H.-U. Habermeier, J. Maier, Quantitative comparison of mixed conducting SOFC cathode materials by means of thin film model electrodes, J. Electrochem Soc. 154 (2007) B931, https://doi.org/10.1149/1.2752974.

[62] A. Ndubuisi, S. Abouali, K. Singh, V. Thangadurai, Recent advances, practical challenges, and perspectives of intermediate temperature solid oxide fuel cell cathodes, J. Mater. Chem. A Mater. 10 (2022) 2196–2227, https://doi.org/10.1039/d1ta08475e.

[63] L. Dos Santos-Gómez, S. Sanna, P. Norby, N. Pryds, E.R. Losilla, D. Marrero-López, V. Esposito, Electrochemical stability of (La,Sr)CoO3-δ in (La,Sr)CoO3-δ /(Ce,Gd)O2-delta; Heterostructures, Nanoscale 11 (2019) 2916–2924, https://doi.org/10.1039/c8nr08528e.

[64] Y.H. Lee, H. Ren, E.A. Wu, E.E. Fullerton, Y.S. Meng, N.Q. Minh, All-sputtered, superior power density thin-film solid oxide fuel cells with a novel nanofibrous ceramic cathode, Nano Lett. 20 (2020) 2943–2949, https://doi.org/10.1021/acs.nanolett.9b02344.

[65] J. Yoon, S. Cho, J.H. Kim, J. Lee, Z. Bi, A. Serquis, X. Zhang, A. Manthiram, H. Wang, Vertically aligned nanocomposite thin films as a cathode/electrolyte interface layer for thin-film solid oxide fuel cells, Adv. Funct. Mater. 19 (2009) 3868–3873, https://doi.org/10.1002/adfm.200901338.

[66] M.B. Hanif, J.T. Gao, K. Shaheen, Y.P. Wang, M. Yasir, S.L. Zhang, C.J. Li, C.X. Li, Performance evaluation of highly active and novel $La_{0.7}Sr_{0.3}Ti_{0.1}Fe_{0.6}Ni_{0.3}O_{3-\delta}$ material both as cathode and anode for intermediate-temperature symmetrical solid oxide fuel cell, J. Power Sources 472 (2020), https://doi.org/10.1016/j.jpowsour.2020.228498.

[67] D. Marrero-López, R. Romero, F. Martín, J.R. Ramos-Barrado, Effect of the deposition temperature on the electrochemical properties of $La_{0.6}Sr_{0.4}Co_{0.8}Fe_{0.2}O_{3-\delta}$ cathode prepared by conventional spray-pyrolysis, J. Power Sources 255 (2014) 308–317, https://doi.org/10.1016/j.jpowsour.2014.01.021.

[68] S. Hwang, M. Choi, J. Lee, G. Kang, S.J. Kim, B. Seong, H. Lee, W. Lee, D. Byun, Infiltrated thin film structure with hydrogel-mediated precursor ink for durable SOFCs, Sci. Rep. 11 (2021), https://doi.org/10.1038/s41598-021-86572-w.

[69] D.A. Osinkin, An approach to the analysis of the impedance spectra of solid oxide fuel cell using the DRT technique, Electro Acta 372 (2021) 137858, https://doi.org/10.1016/j.electacta.2021.137858.

[70] D.A. Osinkin, Detailed analysis of electrochemical behavior of high–performance solid oxide fuel cell using DRT technique, J. Power Sources 527 (2022), https://doi.org/10.1016/j.jpowsour.2022.231120.

[71] J. Zamudio-García, J.M. Porras-Vázquez, E.R. Losilla, D. Marrero-López, Efficient symmetrical electrodes based on $LaCrO_3$ via microstructural engineering, J. Eur. Ceram. Soc. 42 (2022) 181–192, https://doi.org/10.1016/j.jeurceramsoc.2021.09.059.